

# Moiré in $\Gamma$ -valley square lattice: Copper- and iron-based superconductor simulation in a single device

Toshikaze Kariyado,<sup>1</sup> Yusuf Wicaksono,<sup>1</sup> Ashvin Vishwanath,<sup>2</sup> Pavel Volkov,<sup>3</sup> and Zhu-Xi Luo<sup>4</sup>

<sup>1</sup>*International Center for Materials Nanoarchitectonics (WPI-MANA),  
National Institute for Materials Science, Tsukuba 305-0044, Japan*

<sup>2</sup>*Department of Physics, Harvard University, Cambridge, MA 02138, USA*

<sup>3</sup>*Department of Physics, University of Connecticut, Storrs, Connecticut 06269, USA*

<sup>4</sup>*School of Physics, Georgia Institute of Technology, Atlanta, Georgia 30332, USA*

(Dated: March 13, 2026)

Novel superconducting phases have been found in various moiré heterostructures based on hexagonal lattices. However, the archetypal high-temperature superconductors (cuprates, iron-based and nickelate families) all share a square lattice foundation. These materials host a rich landscape of correlated phenomena, such as charge and spin stripes, pseudogap behavior, and unconventional metallicity, which continue to challenge our fundamental understanding of strongly correlated electrons. In this work, we investigate the possibility of simulating the effective models governing these high- $T_c$  superconductors using twisted homobilayers of  $\Gamma$ -valley square-lattice systems. We develop a universal theoretical framework and carry out a detailed analysis of a promising candidate material  $\text{ZnF}_2$ . We find that the first moiré band realizes a single-orbital square-lattice Hubbard model, widely believed to capture cuprate physics, while the second and third moiré bands map to a  $p_x, p_y$  two-orbital square-lattice Hubbard model, which shares common physics to the minimal  $d_{xz}, d_{yz}$  models proposed for iron pnictides. Our study combines continuum Hamiltonian modeling, first-principle calculations, and Hartree-Fock mean field theory. The latter focuses on the quarter-filling regime of the two-orbital model and in particular leads to, among others, a stable antiferro-orbital, ferromagnetic insulating phase. These results highlight  $\Gamma$ -valley square-lattice moiré systems as a new and important generation of van der Waals heterostructures to realize interesting strongly correlated phases of matter.

## CONTENTS

I. Introduction	1
II. Gamma point material	2
A. The hopping parameters	3
B. The Coulomb interactions	3
C. Antiferro-Orbital Order	3
III. Twisted bilayer $\text{ZnF}_2$	4
A. Modeling from first-principle calculations	4
B. Band structures	5
C. Hubbard parameters	5
D. Symmetry breaking orders	5
IV. Discussions	7
Acknowledgments	8
Appendices	8
A. Asymptotic expansion of Mathieu functions	8
B. Quartic interactions	8
C. DFT calculation details	11
D. Coulomb interactions in $\text{ZnF}_2$	12
E. Hartree-Fock details	12
References	14

## I. INTRODUCTION

Moiré heterostructures of van der Waals (vdW) materials have proven to be powerful and versatile platforms to simulate important models in condensed matter physics as well as to generate novel strongly correlated quantum phenomena. While rich correlated physics has been revealed in moiré systems — especially superconductivity [1–11] — research has so far focused almost exclusively on hexagonal lattices. In contrast, the canonical high-temperature superconductors—cuprates [12], iron-based superconductors [13, 14], and most recently the nickelate families [15] — all share a square-lattice foundation. These materials exhibit unconventional superconductivity intertwined with strongly correlated phenomena such as charge and spin stripes, pseudogap behavior, and exotic metallicity—features that remain among the most profound challenges in condensed matter physics. Their intrinsic chemical complexity and limited tunability have long obscured the underlying microscopic mechanisms. Given the exceptional tunability of vdW heterostructures, square-lattice moiré platforms provide a promising route to emulate the essential physics of high- $T_c$  superconductors, offering a clean and controllable reference system to understand these materials and potentially uncover new correlated phenomena beyond them.

Twisted square lattices have been discussed theoretically in several references [16–19]. However, these studies emphasize single-particle flat bands at small twist angles, leaving interaction-driven physics and material

realizations largely unexplored. Material-specific efforts have targeted heterostructures of monolayer superconductors to engineer novel phases of matter [20–25], distinct from the goal of controllably simulating strongly correlated physics in the high- $T_c$  families themselves using non-superconducting parent layers. Analog implementations in cold atoms [26–28], optical [29–31], and acoustic [32] systems have also explored square-lattice geometries, but vdW platforms offer unique advantages in interaction strength and tunability at moderate temperatures.

Attempts to simulate the high- $T_c$  superconductor physics has also been made. Ref. [33] by some of the authors established a theoretical framework for twisted homobilayers of square lattices, where the parent layer band extremum is at the Brillouin zone corner ( $M$ -valley). The follow-up work [34] analyzed a candidate material,  $C_{568}$ , which hosts many of the ideal properties for such systems but remains experimentally unrealized as of now.

Research on  $\Gamma$ -valley square-lattice systems is even more sparse [25, 35] and a general framework is yet unavailable. This work will close this gap through a systematic study of the continuum model and the resultant effective Hubbard-type model on the moiré superlattice, and further examine  $ZnF_2$  as a promising candidate. Interestingly, the first moiré band is found to realize the single-orbital square lattice Hubbard model which is widely believed to capture essential cuprate physics [12], while the following two moiré bands are found to realize two-orbital square lattice Hubbard models closely related to the effective  $d_{xz}$ ,  $d_{yz}$ -models proposed for iron pnictides [36–38]. Although these models use different symmetry assignments from the microscopically accurate models [39, 40], leading to different Fermi surface topology in a symmetry extended Brillouin zone, they are still believed to capture key qualitative aspects of the relevant physics of the [41, 42]. The moiré realization is demonstrated in the general theoretical analysis in section II and further supported by first-principle calculations in the twisted homobilayer of  $ZnF_2$  in section III, along with new Hartree-Fock calculations for the two-orbital model at quarter filling, which could be of separate interest.

## II. GAMMA POINT MATERIAL

When the monolayer material has band extremum at the  $\Gamma$  point, the symmetry-permitted effective twisted bilayer Hamiltonian reads [33]

$$H = \begin{pmatrix} H_0(-i\nabla_{+\theta/2}) + V(\mathbf{x}) & T(\mathbf{x}) \\ T(\mathbf{x})^* & H_0(-i\nabla_{-\theta/2}) + V(\mathbf{x}) \end{pmatrix}, \quad (1)$$

where the intralayer kinetic energy is  $H_0(-i\nabla_{\pm\theta/2}) = \frac{\hbar^2}{2m^*}(-i\nabla_{\pm\theta/2})^2$ , with  $m^*$  being the effective mass. We have neglected spin-orbit coupling which vanishes at the  $\Gamma$ -point and is completely absent in presence of inversion (such as in the case of  $ZnF_2$  studied below) at the single-

layer level. Lattice periodicity ensures that  $V(\mathbf{x})$  is a periodic function and time reversal symmetry constrains it to be real. Fourfold rotation  $C_{4z}$  require that  $V(\mathbf{x}) = V(C_{4z}\mathbf{x})$ , and reflection symmetries with respect to the  $x$ -axis requires  $V(x, y) = V(-x, y)$ . Similar constraints apply to the interlayer hopping  $T(\mathbf{x})$  as well. To the lowest harmonics, we thus have

$$\begin{aligned} V(\mathbf{x}) &= V_1 [\cos(\mathbf{g}_1 \cdot \mathbf{x}) + \cos(\mathbf{g}_2 \cdot \mathbf{x})], \\ T(\mathbf{x}) &= T_0 + T_1 [\cos(\mathbf{g}_1 \cdot \mathbf{x}) + \cos(\mathbf{g}_2 \cdot \mathbf{x})], \end{aligned} \quad (2)$$

where  $\mathbf{g}_1, \mathbf{g}_2$  are the moiré reciprocal lattice vectors of magnitude  $|\mathbf{g}_i| = \frac{2\pi}{a_m}$  with moiré lattice constant  $a_m \approx a_0/\theta$ . At small twisting angles, the difference between  $H_0(-i\nabla_{\pm\theta/2})$  can be ignored such that the Hamiltonian can be diagonalized in the  $\sigma^x$  basis, and consequently separation of variables is possible:  $H_{\pm} = H_{\pm,x} + H_{\pm,y}$ , where

$$H_{\pm,x_i} = H_0(-i\nabla_i) \pm \frac{1}{2}T_0 + (V_1 \pm T_1) \cos(g_i x_i). \quad (3)$$

After variable separation along  $\mathbf{g}_1, \mathbf{g}_2$  directions, the corresponding one-dimensional single-particle Schrödinger equation has the form of 1D Mathieu equations (see for example [43]).

$$\frac{d^2}{dX_i^2} \psi_{\pm,i}(X_i) + [A_{\pm} - 2B_{\pm} \cos(2X_i)] \psi_{\pm,i}(X_i) = 0, \quad (4)$$

where we have re-parametrized  $X_i = \frac{\pi}{a_m} x_i$ ,  $A_{\pm} = \frac{m^*}{\hbar^2} \frac{a_m^2}{\pi^2} (2E_{\pm,i} \mp T_0)$  and  $B_{\pm} = + \frac{m^* a_m^2}{\hbar^2 \pi^2} (V_1 \pm T_1)$ . The full eigenenergies are given by  $E_{\pm} = E_{\pm,x} + E_{\pm,y}$ . Without loss of generality, we focus on the  $-$  branch, omit the subscript in  $A, B$  and assume  $B > 0$ , but alternative choices can be analyzed using similar methods. Solutions to (4) are the cosine- and sine-elliptic Mathieu functions, see table I. When  $B > 0$ , the eigenvalues satisfy the rela-

Eigenvalue	Eigenfunction	Period	Parity
$a_{2n}(B)$	$ce_{2n}(B, X_i)$	$\pi$	Even
$a_{2n+1}(B)$	$ce_{2n+1}(B, X_i)$	$2\pi$	Even
$b_{2n+1}(B)$	$se_{2n+1}(B, X_i)$	$2\pi$	Odd
$b_{2n+2}(B)$	$se_{2n+2}(B, X_i)$	$\pi$	Odd

TABLE I. Solutions to Mathieu equation.

tions  $a_0 < b_1 < a_1 < b_2 < a_2 < b_3 \dots$ . At the moiré  $\Gamma_m$  point, the Bloch wavefunction is  $\pi$ -periodic, so we are only interested in the eigenvalues with even subscripts. The ground state will have energy  $\varepsilon_s(\Gamma_m) = 2a_0$ , while the first and second excited states are degenerate with energy  $\varepsilon_{p_x}(\Gamma_m) = \varepsilon_{p_y}(\Gamma_m) = a_0 + b_2$ , since we can have  $a_0$  in the  $X$  direction,  $b_2$  in the  $Y$  direction or vice versa. As for the  $M_m$  point at the moiré Brillouin zone corner, the Bloch wavefunction is  $2\pi$ -periodic. The ground state at this point has energy  $\varepsilon_s(M_m) = 2b_1$ , the first and second excited states have energy  $\varepsilon_{p_x}(M_m) = \varepsilon_{p_y}(M_m) = a_1 + b_1$  and is again twofold degenerate. At the  $X_m$  ( $Y_m$ )

point, the Bloch wavefunction is  $\pi$ -periodic in the  $y$  ( $x$ )-direction, but  $2\pi$  periodic in the  $x$  ( $y$ )-direction. The lowest energy is  $\varepsilon_s(X_m) = a_0 + b_1$ , and we further have excited state energies  $\varepsilon_{p_x}(X_m) = \varepsilon_{p_y}(Y_m) = a_0 + a_1$  and  $\varepsilon_{p_y}(X_m) = \varepsilon_{p_x}(Y_m) = b_1 + b_2$ .

In the asymptotic limit of  $\theta \rightarrow 0$  or equivalently  $B \rightarrow \infty$ , physically intuitive analytical expressions can be obtained. We will analyze the three lowest energy bands and the resultant effective Hubbard-type models.

### A. The hopping parameters

When  $\theta \rightarrow 0$ , it's natural to keep only the hopping between nearest neighbors on the moiré superlattice, leading to dispersion  $\varepsilon_s(\mathbf{k}) = E_s - 2t(\cos k_x + \cos k_y)$ . The hopping amplitude can thus be obtained from  $t \propto [\varepsilon_s(M_m) - \varepsilon_s(\Gamma_m)]/8$  and using the asymptotic forms of  $a_0$  and  $b_1$ , we have

$$t \sim \frac{\hbar^2 \pi^2}{m_* a_m^2} \frac{8\sqrt{2}}{\sqrt{\pi}} B^{\frac{3}{4}} e^{-4\sqrt{B}}, \quad (5)$$

see Appendix IV A for details. Similar results have also been obtained in the context of tight-binding tunneling amplitude in an optical lattice [43].

The next two lowest bands correspond to the  $p_x, p_y$  orbitals, with dispersions  $\varepsilon_{p_x} = E_p - 2t_\sigma \cos k_x - 2t_\pi \cos k_y$ , and  $\varepsilon_{p_y} = E_p - 2t_\pi \cos k_x - 2t_\sigma \cos k_y$ , respectively. For concreteness we will assume the hopping parameters satisfy  $t_\sigma < t_\pi$ . The two hopping parameters can be extracted from  $t_\sigma \propto [\varepsilon_{p_x}(X_m) - \varepsilon_{p_x}(\Gamma_m)]/4 = (a_1 - b_2)/4$ ,  $t_\pi \propto [\varepsilon_{p_x}(Y_m) - \varepsilon_{p_x}(\Gamma_m)]/4 = (b_1 - a_0)/4$ . Using asymptotic expansion of these characteristic values, we obtain

$$t_\pi \sim t, \quad t_\sigma \sim -16B^{1/2}t_\pi. \quad (6)$$

Notably,  $t_\sigma$  and  $t_\pi$  have opposite signs and scale differently. While it is omitted in this work, one can also repeat similar calculations for even higher bands of  $d$ -,  $f$ -orbitals etc., which can also be easily accessed in experiments via gating.

### B. The Coulomb interactions

To further estimate the Coulomb interactions in the effective moiré Hubbard-type models, we expand the periodic potential near its minima to quadratic order. Upon separation of variables and dropping an irrelevant constant  $T_0/2$ , the Hamiltonian becomes

$$H_{\pm, x_i} \rightarrow -\frac{\hbar^2}{2m_*} \partial_i^2 + \frac{1}{2} m_* \omega_{\pm}^2 x_i^2 \quad (7)$$

where we have identified  $\omega_{\pm} = g\sqrt{|V_1 \pm T_1|/m_*}$ . Further denoting  $\alpha_{\pm} = m_* \omega_{\pm}/\hbar$ , the lowest-energy wavefunctions are  $\psi_s = \sqrt{\alpha/\pi} e^{-\alpha(x^2+y^2)/2}$ , and  $\psi_{p_i} =$

$\sqrt{2/\pi} \alpha x_i e^{-\alpha(x^2+y^2)/2}$ . It is then straightforward to compute the density-density interactions between orbitals  $o$  and  $o'$  with separation  $\mathbf{d}$ :

$$\frac{4\pi\epsilon}{e^2} U_{oo'}(\mathbf{d}) = \int d\mathbf{x} d\mathbf{x}' \frac{1}{2|\mathbf{x} - \mathbf{x}'|} \psi_o^2(\mathbf{x} - \mathbf{d}) \psi_{o'}^2(\mathbf{x}') \quad (8)$$

For the ground state, the integral (8) evaluates to be

$$U_{ss}(\mathbf{d}) = \frac{e^2}{4\pi\epsilon} \frac{\sqrt{\pi\alpha}}{2\sqrt{2}} I_0(\alpha d^2/4) e^{-\alpha d^2/4}, \quad (9)$$

where  $I$  is the modified Bessel function of the first kind.  $U_{ss}(\mathbf{d})$  decays as  $\sim 1/d$  as expected. When  $d \rightarrow 0$ , we obtain the onsite contribution

$$U_{ss}(0) = \frac{e^2}{4\pi\epsilon} \frac{\sqrt{\pi\alpha}}{2\sqrt{2}}. \quad (10)$$

Consistent results were obtained in ref.[33] in a different context. For excited states, (8) leads to (details are in appendix IV B)

$$U_{p_x p_x}(0) = \frac{25}{32} U_{ss}(0), \quad U_{p_x p_y}(0) = \frac{19}{32} U_{ss}(0). \quad (11)$$

It's also easy to evaluate that the onsite Hund's coupling is  $J_{p_x p_y}(0) = \frac{3}{16} U_{ss}(0)$ , which is even smaller than  $U_{p_x p_y}$ .

We would like to point out that while the harmonic oscillator approximation is powerful in estimating the Coulomb interactions in the asymptotic limit, it gives wrong pre-exponential as well as exponential factors [43] for hopping parameters, which is why we chose to use the Mathieu function treatment in section II A instead.

### C. Antiferro-Orbital Order

In this section, we focus on the  $p_x, p_y$ -orbitals and examine the orderings at quarter filling. In the asymptotic limit of strong coupling, large on-site Coulomb interactions strictly enforce single-site occupancy, localizing the charges. Because the inter-site hoppings decay exponentially with respect to the moiré lattice constant  $a_m$ , while the inter-site Coulomb interactions only decrease as a power law, the system operates in a hierarchy of scales where nearest-neighbor Coulomb repulsions dominate over the kinetic energy. Consequently, the leading-order physics is driven by classical electrostatics, which dictates the orbital configuration. Because virtual hopping processes (superexchange) are exponentially suppressed relative to these interactions, we neglect them at this zeroth-order level, leaving the spin degrees of freedom macroscopically degenerate. We will therefore examine the orbital arrangements by taking into account only the nearest neighbor Coulomb interactions.

The energies of the three orbital arrangements in fig. 1, corresponding to ferro-orbital, stripe-orbital and antiferro-orbital order will be examined. For convenience we introduce the following conventions:  $U_A \equiv$

$U_{p_x p_x}(a_m, 0) = U_{p_y p_y}(0, a_m)$ ,  $U_B \equiv U_{p_x p_y}(a_m, 0) = U_{p_x p_y}(0, a_m)$ , and  $U_C \equiv U_{p_x p_x}(0, a_m) = U_{p_y p_y}(a_m, 0)$ , whose expressions have been derived in appendix IV B. One can then check that the energy per atom for the three arrangements in fig. 1 are:

$$\begin{aligned} E^{(a)} &= U_A + U_C, & E^{(c)} &= 2U_B, \\ E^{(b)} &= U_B + (U_A + U_C)/2. \end{aligned} \quad (12)$$

From the asymptotic expansions of  $U$ 's, it can be calculated that

$$U_A + U_C - 2U_B \sim \frac{57}{8\alpha^2 d^5}. \quad (13)$$

Therefore,  $2U_B < U_A + U_C$  is always satisfied, which further leads to  $E^{(a)} > E^{(b)} > E^{(c)}$  - the antiferro-orbital order is always favored at small twisting angles.

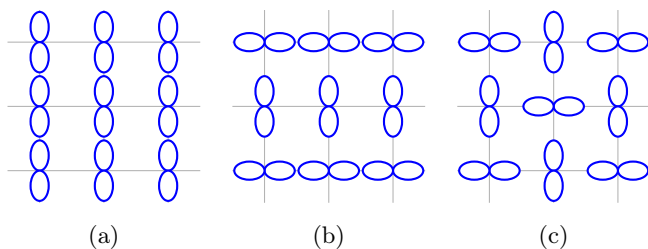


FIG. 1. Orbital configurations for (a) ferro-orbital order, (b) stripe-orbital order, and (c) antiferro-orbital order.

### III. TWISTED BILAYER $\text{ZnF}_2$

$\text{ZnF}_2$  is a two-dimensional van der Waals material on square lattice. It was identified in first-principle calculations [44, 45] as computationally stable and twistable, and exfoliable from the 3D parent  $[\text{NH}_4]_2\text{ZnF}_4$  [46]. The crystal structure is shown in fig. 2 with space group  $P4/mmm$  and lattice constant 3.87 Ångström.

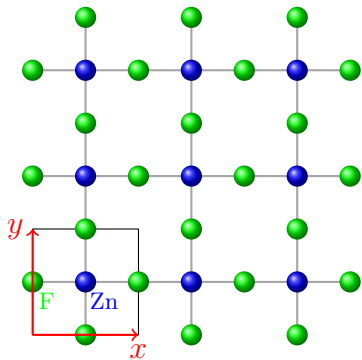


FIG. 2. Crystal structure of monolayer  $\text{ZnF}_2$ .

We will focus on the conduction band minimum which resides at the  $\Gamma$  point and the dominant orbital is Zn

4s. In contrast, the valence band top is at the  $M$ -point and the relevant orbitals are the Zn  $d_{x^2-y^2}$  and F  $p_x, p_y$  orbitals, which are all in-plane and produce only weak moiré effect (bilayer band structures for different relative stackings do not show clear moiré modulations). The monolayer band structure and orbital details can be found in Appendix IV C.

#### A. Modeling from first-principle calculations

To fit the parameters in the symmetry-allowed moiré potentials defined in (1) from first-principle calculations, we approximate the local twisted bilayer environment by untwisted bilayers with different relative constant shifts, see appendix IV C for details. For each shift  $\tau$ , we vary the total bilayer energy as a function of interlayer distances to find the optimal  $d_z(\tau)$  associated with the lowest total energy. The band structure calculation for the untwisted bilayer is then performed with the optimal  $d_z(\tau)$ . The difference between the conduction band minima for the lowest and second lowest conduction bands is twice  $T[\tau(\mathbf{x})]$ , and the average of these two energies lead to  $V[\tau(\mathbf{x})]$ .

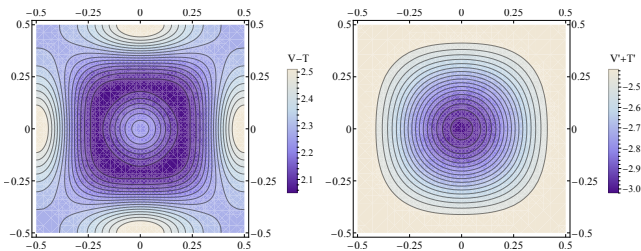


FIG. 3. Real-space profiles for moiré potentials of twisted bilayer  $\text{ZnF}_2$  in equation (1), plotted as a function of normalized coordinates within the moiré unit cell in eV. Left: corrugated case where the interlayer distance  $d_z$  is a function of the relative displacement  $\tau$  (left,  $V - T$ ). Right: rigid case, where  $d_z$  taken to be a constant, the spatial average of the corrugated case (right,  $V' + T'$ ). The corrugation splits the moiré potential minimum from one point at the unit cell center to four points.

In fig. 3 we plot the combination of the moiré potential  $V(\mathbf{x}) - T(\mathbf{x})$  responsible for the moiré band structures. The left and right panels contrast the cases with and without corrugation. For the rigid, constant  $d_z$  case, interlayer tunneling is expected to be large at  $\tau = 0$ , where the distance between the sites in the two layers is the smallest. The situation changes when  $d_z$  is allowed to vary, leading to the splitting of the moiré potential minimum in the left panel. The first several harmonics of the moiré potentials in the corrugated case are presented in table II (see appendix IV C for details).

	$n = 1$	$n = 2$	$n = 3$	$n = 4$	$n = 5$
$V_n$	-40.17013	-55.305	10.8649	15.7927	4.58234
$T_n$	-3.42321	-23.6122	-17.0831	-14.7755	-1.42366

TABLE II. Fitted strengths of the moiré potentials in the twisted bilayer Hamiltonian for the  $n$ -th harmonics, in units of meV. As for the constant terms,  $V_0 = 2.87056$  eV and  $T_0 = 0.628548$  eV. The fact that  $|T_1| < |T_2|$  originates from the corrugation - the rigid case leads to  $|T_1| > |T_2|$  instead.

### B. Band structures

Band structures of the twisted bilayer model in equations (1)(43) for twisting angles  $1^\circ$  and  $2^\circ$  are shown in fig. 4. The gap between the lowest and neighboring moiré conduction bands is of order 10 meV and therefore the higher bands can easily be accessed via gating. Zooming

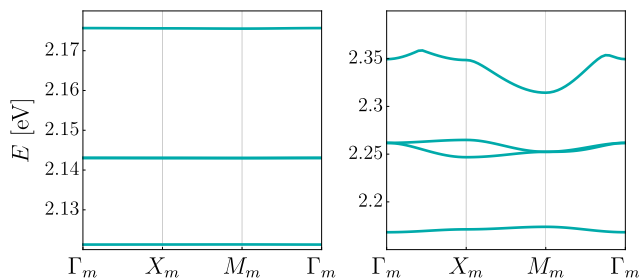


FIG. 4. Moiré band structures at twisting angle  $\theta = 1^\circ$  (left) and  $\theta = 2^\circ$  (right).

in near the lowest moiré conduction band and the next two low-lying bands, we see in fig. 5 that they manifest the  $s$ - and  $p_x, p_y$  orbital physics consistent with the discussions in section II.

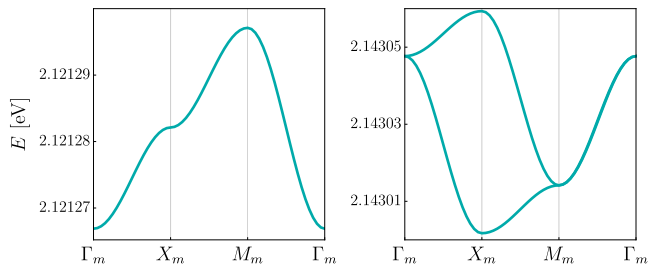


FIG. 5. Band structures at  $\theta = 1^\circ$ . Left: the lowest-lying band corresponding to moiré  $s$ -orbital. Right: the next two low-lying bands corresponding to the moiré  $p_x, p_y$  orbitals.

### C. Hubbard parameters

As shown in figure 4, the lowest moiré bands are well-isolated from the other bands, it is therefore justified to have reasonably localized Wannier orbitals. We first obtain the Bloch wave functions for these lowest bands us-

ing the continuum bilayer Hamiltonian (fully accounting for the harmonics presented in II). Because numerical solvers assign arbitrary, momentum-dependent phases to these Bloch states, a direct Fourier transform would yield unphysical orbitals. To resolve this ambiguity, we project the raw Bloch states onto localized, ansatz Gaussian functions. Aligning the Bloch states to this smooth phase reference allows us to successfully construct the physically localized Wannier orbitals used in our model. This procedure is equivalent to the projection on initial guess functions in ref. [47]. We plot the real-space distributions of the Wannier functions. in the left panel of Fig. 6. The right panel shows the hopping parameters derived from Wannier function overlaps.

The matrix elements for onsite Coulomb interactions and exchange can further be estimated by integrating over the Wannier functions, see for example refs. [34, 48] and the appendix IV D for details. Without specification of the substrate, it is hard to estimate the screening, so we have therefore chosen a typical value of dielectric constant  $\epsilon = 10$  and plot the resultant interactions in figs. 7, as functions of twisting angle. We however remark that the screening can be tuned via gate separation [49]. The onsite Coulomb interactions are typically of order 50 meV, significantly larger than the hopping parameters. However, as the twisting angle is increased, the bandwidth can cross the Coulomb interaction, potentially driving a metal-insulator transition. The next-nearest neighbor Coulomb interaction details can be found in the Appendix IV D, consistently showing the  $2U_B < U_A + U_C$  observed in section II C.

### D. Symmetry breaking orders

In this subsection, we will explore the possible symmetry-breaking phases in the  $p$ -orbitals. The relevant moiré Hamiltonian is

$$\begin{aligned}
 H_p = & -t_\sigma \sum_{i,\sigma} (c_{i,p_x\sigma}^\dagger c_{i+\hat{x},p_x\sigma} + c_{i,p_y\sigma}^\dagger c_{i+\hat{y},p_y\sigma}) + \text{h.c.} \\
 & -t_\pi \sum_{i,\sigma} (c_{i,p_x\sigma}^\dagger c_{i+\hat{y},p_x\sigma} + c_{i,p_y\sigma}^\dagger c_{i+\hat{x},p_y\sigma}) + \text{h.c.} \\
 & + \frac{1}{2} \sum_{i,o,\sigma} \left[ U n_{i,o\sigma} n_{i,o\bar{\sigma}} - J c_{i,o\sigma}^\dagger c_{i,\bar{o}\bar{\sigma}} c_{i,\bar{o}\bar{\sigma}}^\dagger c_{i,o\sigma} \right. \\
 & \left. + \sum_{\sigma'} \left( U' n_{i,o\sigma} n_{i,\bar{o}\sigma'} - J c_{i,o\sigma}^\dagger c_{i,\bar{o}\sigma'} c_{i,\bar{o}\sigma'}^\dagger c_{i,o\sigma} \right) \right], \tag{14}
 \end{aligned}$$

where  $\bar{\uparrow} = \downarrow, \bar{\downarrow} = \uparrow$  for spins  $\sigma$  and  $\bar{p}_x = p_y, \bar{p}_y = p_x$  for orbitals  $o$ . This model has been studied at half filling in the context of iron-pnictide superconductors (where the Fe  $d_{xz}$  and  $d_{yz}$  orbitals lead to a minimal two-orbital model with hopping structure equivalent to that of  $p_x, p_y$  orbitals here), which can capture important features of the family such as Fermi surface structure and mag-

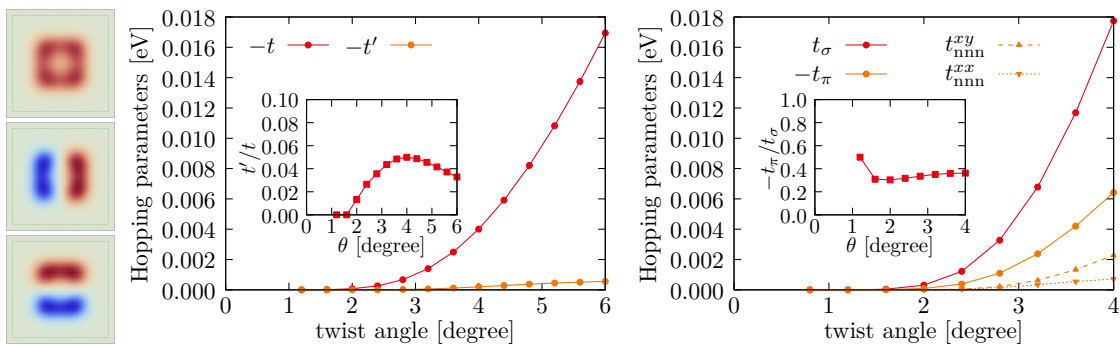


FIG. 6. Left: real-space distributions of the Wannier functions for the  $s$ ,  $p_y$  and  $p_x$  orbitals. Middle:  $s$ -orbital hopping parameters for nearest neighbor  $t$  and next nearest neighbor  $t'$ . Inset: Ratio  $t'/t$  as a function of twisting angle  $\theta$ . Right:  $p_x$ ,  $p_y$ -orbital hopping parameters for nearest neighbor  $t_\sigma$ ,  $t_\pi$  and next nearest neighbor  $t^{xy}$  and  $t^{xx}$ . Inset: Ratio  $-t_\pi/t_\sigma$  as a function of  $\theta$ .

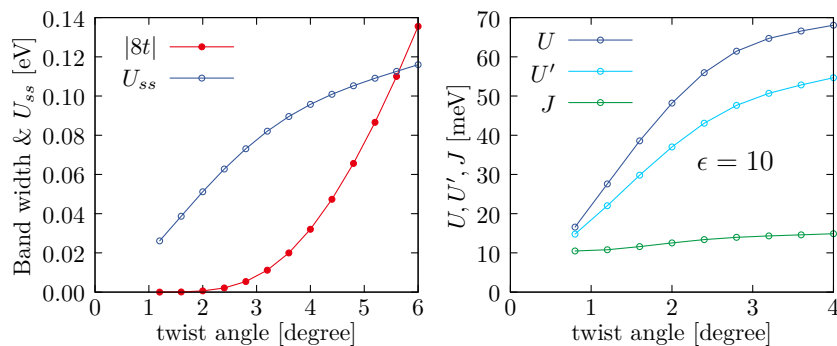


FIG. 7. Left: Onsite Coulomb interaction in the  $s$ -orbital  $U_{ss}(0)$  as a function of twisting angle and comparison with bandwidth  $W = |8t|$  (taking into account only the nearest neighbor hopping), plotted in eV. Right panel: For  $p$ -orbitals, strengths of intra-orbital Coulomb  $U = U_{p_x p_x}(0) = U_{p_y p_y}(0)$ , inter-orbital Coulomb  $U' = U_{p_x p_y}(0)$  and Hund's coupling  $J$ , plotted in meV.

netic orderings [36–38]. The low-dimensional vdW heterostructure allows for easy access to other fillings, and in this subsection the case of quarter filling will be examined using self-consistent Hartree-Fock mean field theory. Numerical details of the calculation can be found in Appendix IVE, and in figure 8 we show the phase diagram consisting of three distinct phases separated by first-order transitions: at  $2.4^\circ \leq \theta \leq 4.6^\circ$ , the system is gapped and exhibits antiferro-orbital (AFO) ordering with checkerboard pattern, and ferromagnetic spin ordering. The emergence of the AFO+FM order can be intuitively understood from the effective spin-orbital model in the strong-coupling regime: the orbital superexchange scale  $t^2/U'$  dominates over the spin superexchange  $t^2/U$ , favoring staggered orbital ordering, and the Hund's coupling selects spin alignment. This is compatible with and complementary to the analysis of section III C in the asymptotic limit, where the onsite Coulomb interactions are irrelevant and only nearest neighbor Coulomb interaction was taken into account.

Beyond  $\theta > 4.6^\circ$ , the quasiparticle gap is closed. In the range of  $4.6^\circ < \theta < 4.9^\circ$ , the system favors stripe geometry with both finite average and staggered magnetizations, which could be due to strong competitions between

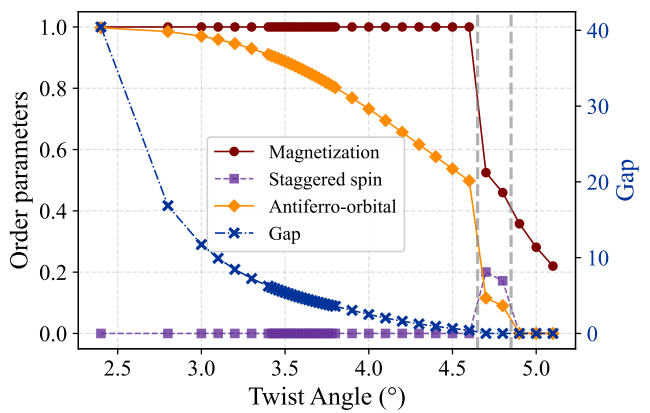


FIG. 8. Order parameters and gap between filled and empty bands as a function of twisting angle. The region with the densest data points correspond to the parameter regime where  $U > U' > t_\sigma$  but all three are of the same order. When there are two sublattices  $A, B$  per unit cell, magnetization is defined as  $|\vec{S}_A + \vec{S}_B|/2$ , staggered spin is defined as  $|\vec{S}_A - \vec{S}_B|/2$ , and antiferro-orbital order  $\sum_\sigma (n_{A p_x \sigma} + n_{B p_y \sigma} - n_{A p_y \sigma} - n_{B p_x \sigma})$ .

the kinetic and interaction interactions. As for  $\theta \geq 4.9^\circ$ ,

the orbital degrees of freedom is disordered, and the spin degrees of freedom still exhibit fast-decaying, small but finite magnetization. It is expected that at even larger twisting angles, the system will become trivial symmetric metal. We have focused on the regime of  $\theta \geq 2.4^\circ$  because at  $2.4^\circ$  the ratio  $U/t_\sigma = 76.43$ , and even larger ratio is expected at even smaller twisting angles. Such parameter combinations, while achievable in the moiré setup, may not be relevant for the broader family of solid state materials.

The orbital-resolved band structures for the AFO phase when  $\theta \leq 4.6^\circ$  is shown in figure 9 in the folded moiré Brillouin zone. Spin and orbital-resolved plots for the other phases can be found in the appendix IV E).

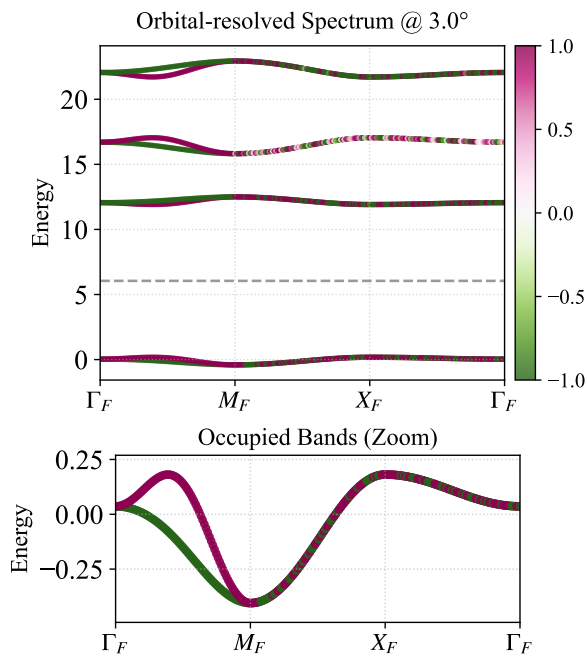


FIG. 9. Orbital-resolved spectrum at  $\theta = 3^\circ$  in the antiferro-orbital phase. Top: all 8 bands in the folded Brillouin zone. Dashed line is the chemical potential. Bottom: zoomed in plot of the two filled bands. The color profile corresponds to the difference between the occupations in the two orbitals. One can further perform sublattice projections, and the pink (green) color only appears in sublattice  $A(B)$ , consistent with the AFO ordering.

#### IV. DISCUSSIONS

This work establishes  $\Gamma$ -valley square-lattice moiré systems as a versatile synthetic platform for simulating foundational models of high- $T_c$  superconductivity. Leveraging the exceptional tunability of van der Waals heterostructures, these devices provide a clean and highly controllable setting to benchmark competing orders and to explore regimes of the Hubbard model that are experimentally inaccessible in conventional bulk materials. No-

tably, our candidate platform can emulate square-lattice cuprate physics: the point  $U \sim 8t$  is reached in the lowest band at a twist angle of approximately  $5^\circ$ , corresponding to the interaction strength widely believed to be relevant for cuprate superconductors (see for example [50]). This connection provides a direct route to realizing  $t-t'-U$  cuprate phenomenology in a moiré system, opening the possibility of observing  $d$ -wave superconductivity and systematically exploring correlated phenomena ranging from the pseudogap regime to strange-metal behavior in a setting where the underlying microscopic parameters can be tuned in situ. Below we discuss a few subtleties and future directions.

In this work, the lowest moiré band and two bands that follow are treated as separate, i.e. potential hybridization has been ignored. In the asymptotic limit, analytical expression for the ratio between onsite  $U_{sp_x}$  and the moiré gap can be estimated, however the result is highly sensitive to the material parameters. In the  $\text{ZnF}_2$  example, at  $\theta = 2^\circ$ , the band gap is of order 50 meV, and the hybridization due to Coulomb interaction is of order 40 meV (see for example figures 4 and 7), so there doesn't seem to be hybridization issue. However, more careful analysis will need to be carried out to give a complete answer to this question, which we leave for future work.

The parameters in the effective models of the moiré system have been estimated using approximations of untwisted bilayers with varying relative shifts between the two layers. This method, however, requires fittings of the band structures. Novel alternative methods which do not require fitting are available have recently been proposed, which can provide complementary perspectives [51].

We comment on the ferromagnetism found in Hartree-Fock calculations in the  $p$ -orbital model. It was proved in ref. [52] that when  $t_\pi = 0$ , in the  $U_{p_x p_x}(0) = U_{p_y p_y}(0) \rightarrow \infty$  limit, at a large range of filling factors, as long as there is nonzero Hund's exchange  $J$ , the ground state exhibits itinerant ferromagnetism. The results (as well as presence of a related antiferro-orbital order) are further confirmed from Quantum Monte Carlo calculation in ref. [53] where the case of finite  $U$  and tiny  $t_\pi/t_\sigma < 0.05$  was also discussed ( $t_\pi$  introduces sign problem and therefore cannot be fully investigated using QMC). In our setup, the ratio  $|t_\pi/t_\sigma| \sim 0.35$  and is therefore beyond the range of existing literature. While unlike the cases in the literature, our antiferro-orbital phase hosts a gap between the filled and empty bands, the system still exhibits ferromagnetism. It is intriguing to carefully examine the relation between this phase and the previous exact results. We note that while our zero-temperature calculations yield a ferromagnetic state, the continuous spin rotation symmetry of the Hamiltonian implies via the Mermin-Wagner theorem that true long-range spin order must melt at finite temperatures. Finally, we will examine the superconductivity phases in the  $p$ -orbital model doped away from quarter-filling in a separate work.

## ACKNOWLEDGMENTS

We are grateful to Junyeong Ahn, Gil Young Cho, Chaoxing Liu, Qimiao Si, Subir Sachdev, Zhida Song, Cenke Xu and Hong Yao for helpful discussions and Shijun Sun for related collaborations. This work was performed in part at the Aspen Center for Physics, which is supported by National Science Foundation grant PHY-2210452. T.K. was supported by JSPS KAKENHI Grant Number JP24K06968. A.V. acknowledges funding from NSF DMR-2220703 and from a Star-Friedman Challenge award at Harvard University.

## APPENDICES

### A. Asymptotic expansion of Mathieu functions

In the asymptotic limit  $B \rightarrow \infty$ , the eigenvalues of the Schrödinger's equation in section II are [54]

$$a_m(B) \sim b_{m+1}(B) \sim -2B + 2(2m+1)\sqrt{B} + \mathcal{O}(1), \quad (15)$$

and

$$b_{m+1}(B) - a_m(B) \sim \frac{2^{4m+5}}{m!} \sqrt{\frac{2}{\pi}} B^{\frac{m}{2} + \frac{3}{4}} e^{-4\sqrt{B}} \times \left(1 + \mathcal{O}(B^{-1/2})\right) \quad (16)$$

Taking  $m = 0$ , this becomes

$$b_1(B) - a_0(B) \sim 32 \sqrt{\frac{2}{\pi}} B^{\frac{3}{4}} e^{-4\sqrt{B}} + \dots \quad (17)$$

Taking  $m = 1$ , this is

$$b_2(B) - a_1(B) \sim 2^9 \sqrt{\frac{2}{\pi}} B^{\frac{5}{4}} e^{-4\sqrt{B}} \left(1 + \mathcal{O}(B^{-1/2})\right) \quad (18)$$

### B. Quartic interactions

This Appendix details the evaluation of the Gaussian type integrals to estimate the interactions in the moiré Hubbard-type model, supporting discussions in section II B. We start with the Coulomb interaction in the ground states. Notice

$$\psi_s^2 = \left(\frac{\alpha}{\pi}\right) e^{-\alpha(x^2+y^2)}, \quad (19)$$

For the relevant integral defined in (8).

Change to center of mass and relative coordinates,  $\mathbf{r} = \mathbf{x} - \mathbf{x}'$ ,  $\mathbf{R} = \frac{1}{2}(\mathbf{x} + \mathbf{x}')$  such that

$$\begin{aligned} & \int d\mathbf{x} \int d\mathbf{x}' \frac{1}{2|\mathbf{x} - \mathbf{x}'|} \psi_s^2(\mathbf{x} - \mathbf{d}) \psi_s^2(\mathbf{x}') \\ &= \frac{\alpha^2}{2\pi^2} \int d\mathbf{r} \int d\mathbf{R} \frac{1}{|\mathbf{r}|} e^{-\alpha[(\mathbf{R} - \mathbf{d} - \mathbf{r}/2)^2 + (\mathbf{R} + \mathbf{r}/2)^2]} \\ &= \frac{\alpha^2}{2\pi^2} \int_0^\infty dr \int_0^{2\pi} d\theta e^{-\alpha(d^2 + rd \cos \theta + r^2/2)} \int_0^\infty RdR \int_0^{2\pi} d\phi e^{-\alpha(2R^2 - 2Rd \cos \phi)} \\ &= \frac{\alpha^2}{2\pi^2} e^{-\alpha d^2} \int_0^\infty dr 2\pi I_0(\alpha dr) e^{-\alpha r^2/2} \int_0^\infty RdR 2\pi I_0(2\alpha dR) e^{-2\alpha R^2} \\ &= \frac{\alpha^2}{2\pi^2} e^{-\alpha d^2} \cdot \frac{\sqrt{2\pi}}{\sqrt{\alpha}} \pi e^{\alpha d^2/4} I_0(\alpha d^2/4) \cdot \frac{\pi}{2\alpha} e^{\alpha d^2/2} \\ &= \frac{\sqrt{\pi\alpha}}{2\sqrt{2}} I_0(\alpha d^2/4) e^{-\alpha d^2/4} \end{aligned} \quad (20)$$

where  $I_0$  is the Bessel function of the first kind. So

$$U_{ss}(\mathbf{d}) = \frac{e^2}{4\pi\epsilon} \frac{\sqrt{\pi\alpha}}{2\sqrt{2}} I_0(\alpha d^2/4) e^{-\alpha d^2/4} \quad (21)$$

When  $d \rightarrow 0$ , we obtain the onsite contribution

$$U_{ss}(0) = \frac{e^2}{4\pi\epsilon} \frac{\sqrt{\pi\alpha}}{2\sqrt{2}}. \quad (22)$$

Next we evaluate the intra-orbital Coulomb interaction for first excited states,

$$\psi_{p_i}^2 = \left(\frac{2}{\pi}\right) \alpha^2 x_i^2 e^{-\alpha(x^2+y^2)}. \quad (23)$$

The relevant integral for intra-orbital Coulomb interaction is

$$\begin{aligned} & \int d\mathbf{x} \int d\mathbf{x}' \frac{1}{2|\mathbf{x}-\mathbf{x}'|} \psi_{p_x}^2(\mathbf{x}-\mathbf{d}) \psi_{p_x}^2(\mathbf{x}') \\ &= \frac{4\alpha^4}{2\pi^2} \int dx dx' x'^2 (x-d_x)^2 e^{-\alpha(x^2+d_x^2-2d_x x+x'^2)} \int dy dy' \frac{1}{\sqrt{(x-x')^2+(y-y')^2}} e^{-\alpha(y^2+d_y^2-2y d_y+y'^2)} \end{aligned} \quad (24)$$

Using the identity

$$\frac{1}{\sqrt{(x-x')^2+(y-y')^2}} = \int \frac{d\mathbf{k}}{2\pi} \frac{e^{i\mathbf{k}\cdot(\mathbf{x}-\mathbf{x}')}}{|\mathbf{k}|} \quad (25)$$

Above reduces to

$$\begin{aligned} & \frac{4\alpha^4}{2\pi^2} \int \frac{d\mathbf{k}}{2\pi} \frac{1}{|\mathbf{k}|} \int dx dx' x'^2 (x-d_x)^2 e^{-\alpha(x^2+d_x^2-2d_x x+x'^2)+ik_x(x-x')} \int dy dy' e^{-\alpha(y^2+d_y^2-2y d_y+y'^2)+ik_y(y-y')} \\ &= \frac{4\alpha^4}{2\pi^2} \frac{\pi}{\alpha} \int \frac{d\mathbf{k}}{2\pi} \frac{1}{|\mathbf{k}|} e^{ik_y d_y - k_y^2/2\alpha} \int dx dx' x'^2 (x-d_x)^2 e^{-\alpha(x^2+d_x^2-2d_x x+x'^2)+ik_x(x-x')} \\ &= \frac{4\alpha^4}{2\pi^2} \frac{\pi}{\alpha} \int \frac{d\mathbf{k}}{2\pi} \frac{1}{|\mathbf{k}|} e^{ik_y d_y - k_y^2/2\alpha} \frac{\pi(k_x^2 - 2\alpha)^2}{16\alpha^5} e^{ik_x d_x - k_x^2/2\alpha} \\ &= \int \frac{d\mathbf{k}}{2\pi} \frac{1}{|\mathbf{k}|} e^{i\mathbf{k}\cdot\mathbf{d} - k^2/2\alpha} \frac{(k_x^2 - 2\alpha)^2}{8\alpha^2} \end{aligned} \quad (26)$$

First assume  $\mathbf{d} = (d, 0)$ , i.e. the separation is along the  $x$ -axis. Integral then becomes

$$\begin{aligned} U_A &= \frac{e^2}{4\pi\epsilon} \int \frac{dk}{2\pi} d\theta e^{ikd \cos \theta - k^2/2\alpha} \frac{(k^2 \cos^2 \theta - 2\alpha)^2}{8\alpha^2} \\ &= \frac{e^2}{4\pi\epsilon} \frac{\sqrt{\pi\alpha}}{\sqrt{2}} e^{-\alpha d^2/4} \left[ \frac{7 + \alpha^2 d^4}{16} I_0(\alpha d^2/4) - \frac{6 + \alpha d^2(5 + \alpha d^2(2 + \alpha d^2))}{16\alpha d^2} I_1(\alpha d^2/4) \right] \end{aligned} \quad (27)$$

Next assume  $\mathbf{d} = (0, d)$ . Integral then becomes

$$\begin{aligned} U_C &= \frac{e^2}{4\pi\epsilon} \int \frac{dk}{2\pi} d\theta e^{ikd \sin \theta - k^2/2\alpha} \frac{(k^2 \cos^2 \theta - 2\alpha)^2}{8\alpha^2} \\ &= \frac{e^2}{4\pi\epsilon} \frac{\sqrt{\pi\alpha}}{\sqrt{2}} e^{-\alpha d^2/4} \left[ \frac{7}{16} I_0(\alpha d^2/4) + \frac{\alpha d^2 - 6}{16\alpha d^2} I_1(\alpha d^2/4) \right]. \end{aligned} \quad (28)$$

It is also possible to evaluate the integral for arbitrary  $\mathbf{d} = (d_x, d_y)$  but the result is tedious and not physically intuitive, so we will omit it here. In the onsite  $d \rightarrow 0$  limit, the Coulomb interaction becomes

$$U_{p_x p_x}(0) = \frac{e^2}{4\pi\epsilon} \frac{\sqrt{\pi\alpha}}{\sqrt{2}} \left[ \frac{7}{16} - \frac{6}{128} \right] = \frac{25}{32} \frac{e^2}{4\pi\epsilon} \frac{\sqrt{\pi\alpha}}{2\sqrt{2}}. \quad (29)$$

Next we turn to the inter-orbital interaction  $U_{p_x p_y}$ . Using again the identity (25),

$$\begin{aligned} & \int d\mathbf{x} \int d\mathbf{x}' \frac{1}{2|\mathbf{x}-\mathbf{x}'|} \psi_{p_x}^2(\mathbf{x}-\mathbf{d}) \psi_{p_y}^2(\mathbf{x}') \\ &= \frac{4\alpha^4}{2\pi^2} \int \frac{d\mathbf{k}}{2\pi} \frac{1}{|\mathbf{k}|} \int dx dx' (x-d_x)^2 e^{-\alpha(x^2+d_x^2-2d_x x+x'^2)+ik_x(x-x')} \int dy dy' y'^2 e^{-\alpha(y^2+d_y^2-2y d_y+y'^2)+ik_y(y-y')} \\ &= \frac{4\alpha^4}{2\pi^2} \int \frac{d\mathbf{k}}{2\pi} \frac{1}{|\mathbf{k}|} \cdot \frac{\pi(k_y^2 - 2\alpha)}{4\alpha^3} \frac{\pi(k_x^2 - 2\alpha)}{4\alpha^3} e^{i\mathbf{k}\cdot\mathbf{d} - k^2/2\alpha} \end{aligned} \quad (30)$$

Assume  $\mathbf{d} = (d, 0)$ , i.e. the separation is along the  $x$ -axis. Integral then becomes

$$\begin{aligned} U_B &= \frac{e^2}{4\pi\epsilon} \int \frac{dk}{2\pi} d\theta e^{ikd \cos \theta - k^2/2\alpha} \frac{(k^2 \cos^2 \theta - 2\alpha)(k^2 \sin^2 \theta - 2\alpha)}{8\alpha^2} \\ &= \frac{e^2}{4\pi\epsilon} \frac{\sqrt{\pi\alpha}}{\sqrt{2}} e^{-\alpha d^2/4} \left[ \frac{(4 + \alpha d^2)}{16} I_0(\alpha d^2/4) + \frac{6 + \alpha d^2(2 - \alpha d^2)}{16\alpha d^2} I_1(\alpha d^2/4) \right] \end{aligned} \quad (31)$$

The onsite contribution is straightforward to find

$$U_{p_x p_y}(0) = \frac{19}{32} \frac{e^2}{4\pi\epsilon} \frac{\sqrt{\pi\alpha}}{2\sqrt{2}} \quad (32)$$

To find the orbital ordering in the asymptotic limit, we need to compute

$$\begin{aligned} &U_A + U_C - 2U_B \\ &= \frac{e^2}{4\pi\epsilon} \frac{\sqrt{\pi\alpha}}{\sqrt{2}} e^{-\alpha d^2/4} \left[ I_0(\alpha d^2/4) \left( \frac{7 + \alpha^2 d^4}{16} + \frac{7}{16} - 2 \frac{(4 + \alpha d^2)}{16} \right) \right. \\ &\quad \left. + I_1(\alpha d^2/4) \left( -\frac{6 + \alpha d^2(5 + \alpha d^2(2 + \alpha d^2))}{16\alpha d^2} + \frac{\alpha d^2 - 6}{16\alpha d^2} - 2 \frac{6 + \alpha d^2(2 - \alpha d^2)}{16\alpha d^2} \right) \right] \\ &= \frac{e^2}{4\pi\epsilon} \frac{\sqrt{\pi\alpha}}{\sqrt{2}} e^{-\alpha d^2/4} \frac{1}{16} \left[ (6 - 2\alpha d^2 + \alpha^2 d^4) I_0(\alpha d^2/4) + \frac{1}{\alpha d^2} (-24 - 8\alpha d^2 - \alpha^3 d^6) I_1(\alpha d^2/4) \right] \end{aligned} \quad (33)$$

Perform the asymptotic expansion up to order  $n_* = 5$ ,

$$I_\nu(x) \sim \frac{e^x}{\sqrt{2\pi x}} \sum_{n=0}^{n_*} (-1)^n \frac{\prod_{m=1}^{2n+1} (4\nu^2 - m^2)}{n!(8x)^n}, \quad (34)$$

the result simplifies to, at leading order,

$$U_A + U_C - 2U_B = \frac{e^2}{4\pi\epsilon} \frac{57}{8\alpha^2 d^5} + O(\alpha^{-3} d^{-7}), \quad (35)$$

which is always positive.

We further analyze the hybridization between the  $s$ - and the  $p$ -orbitals. The relevant integral is

$$\begin{aligned} U_{sp_x}(\mathbf{d}) &= \frac{e^2}{4\pi\epsilon} \int d\mathbf{x} \int d\mathbf{x}' \frac{1}{2|\mathbf{x} - \mathbf{x}'|} \psi_{p_x}^2(\mathbf{x} - \mathbf{d}) \psi_s^2(\mathbf{x}') \\ &= \frac{e^2}{4\pi\epsilon} \frac{\alpha^3}{\pi^2} \int dx dx' x'^2 e^{-\alpha(x^2 + d_x^2 - 2d_x x + x'^2)} \int dy dy' \frac{1}{\sqrt{(x - x')^2 + (y - y')^2}} e^{-\alpha(y^2 + d_y^2 - 2y d_y + y'^2)} \\ &= \frac{e^2}{4\pi\epsilon} \frac{\alpha^3}{\pi^2} \int \frac{d\mathbf{k}}{2\pi} \frac{1}{|\mathbf{k}|} \int dx dx' x'^2 e^{ik_x(x - x')} e^{-\alpha(x^2 + d_x^2 - 2d_x x + x'^2)} \int dy dy' e^{ik_y(y - y')} e^{-\alpha(y^2 + d_y^2 - 2y d_y + y'^2)} \\ &= \frac{e^2}{4\pi\epsilon} \frac{\alpha^3}{\pi^2} \int \frac{d\mathbf{k}}{2\pi} \frac{1}{|\mathbf{k}|} \frac{\pi(2\alpha - k_x^2)}{4\alpha^3} e^{id_x k_x - k_x^2/2\alpha} e^{id_y k_y - k_y^2/2\alpha} \frac{\pi}{\alpha}. \end{aligned} \quad (36)$$

In particular the onsite term is

$$U_{sp_x}(0) = \frac{e^2}{4\pi\epsilon} \frac{\alpha^3}{\pi^2} \frac{3\pi^{5/2}}{8\sqrt{2}\alpha^{5/2}} = \frac{3}{4} \frac{e^2}{4\pi\epsilon} \frac{\sqrt{\pi\alpha}}{2\sqrt{2}}, \quad (37)$$

which satisfies  $U_{ss}(0) > U_{p_x p_x}(0) > U_{sp_x}(0) > U_{p_x p_y}(0)$  as expected.

Finally we calculate the other quartic interactions that are not of Coulomb type and will only focus on the onsite contributions. The Hund's coupling is,

$$\frac{4\pi\epsilon}{e^2} J_H(0) = \int d\mathbf{x} \int d\mathbf{x}' \frac{1}{|\mathbf{x} - \mathbf{x}'|} \psi_o^*(x) \psi_{o'}(x) \psi_{o'}^*(x') \psi_o(x') \quad (38)$$

The pair hopping term is

$$\frac{4\pi\epsilon}{e^2} J'(0) = \int d\mathbf{x} \int d\mathbf{x}' \frac{1}{|\mathbf{x} - \mathbf{x}'|} \psi_o^*(x) \psi_{o'}(x) \psi_o^*(x') \psi_{o'}(x') \quad (39)$$

Since all the wavefunctions are real, we have  $J_H = J' \equiv J$ . Taking  $o = p_x, o' = p_y$ , the integral is

$$\begin{aligned}
& \int d\mathbf{x} \int d\mathbf{x}' \frac{1}{|\mathbf{x} - \mathbf{x}'|} \psi_o^*(x) \psi_{o'}(x) \psi_o^*(x') \psi_{o'}(x') \\
&= \frac{4\alpha^4}{\pi^2} \int d\mathbf{x} \int d\mathbf{x}' \frac{1}{|\mathbf{x} - \mathbf{x}'|} x x' y y' e^{-\alpha(x^2+y^2+x'^2+y'^2)} \\
&= \frac{4\alpha^4}{\pi^2} \int \frac{d\mathbf{k}}{2\pi} \frac{1}{|\mathbf{k}|} \int d\mathbf{x} \int d\mathbf{x}' x x' y y' e^{ik_x(x-x') + ik_y(y-y')} e^{-\alpha(x^2+y^2+x'^2+y'^2)} \\
&= \frac{4\alpha^4}{\pi^2} \frac{\pi^2}{16\alpha^6} \int \frac{d\mathbf{k}}{2\pi} \frac{1}{|\mathbf{k}|} k_x^2 k_y^2 e^{-(k_x^2+k_y^2)/2\alpha} \\
&= \frac{4\alpha^4}{\pi^2} \frac{\pi^2}{16\alpha^6} \frac{1}{2\pi} \frac{3\alpha^{5/2} \pi^{3/2}}{4\sqrt{2}} = \frac{3}{16} \frac{\sqrt{\pi\alpha}}{2\sqrt{2}}.
\end{aligned} \tag{40}$$

Therefore  $J_{p_x p_y}(0) = \frac{3}{16} \frac{e^2}{4\pi\epsilon} \frac{\sqrt{\pi\alpha}}{2\sqrt{2}} < U_{p_x p_y}(0)$ .

### C. DFT calculation details

This section explains in more detail the setup for first-principle calculations described in section III. We performed density function theory calculations using the Quantum Espresso package [55, 56] and implemented the VDW-DF2-B86R choice of the exchange-correlation functional for van der Waals forces [57]. Pseudopotentials are of type PBE and from PS library [58, 59]. A thick supercell in the  $z$ -direction of 100 Angstrom is used in order to handle the two-dimensional material. The monolayer band structure and orbital information can be found in figs. 10 and 11.

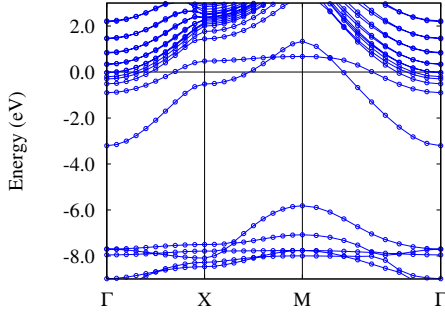


FIG. 10. Monolayer band structure showing conduction band minimum (CBM) at the  $\Gamma$  point and valence band maximum (VBM) at the  $M$  point.

For bilayer, we incorporate the corrugation effects between planes, while assuming a rigid material plane. The optimal interlayer distance modulates in the following symmetry-constrained way:

$$d(\mathbf{x}) = d_0 + \sum_n d_n \left[ \sum_{c=0}^3 \cos(2\pi\mathbf{x} \cdot (C_{4z}^c \cdot \mathbf{v}_n)) \right], \tag{41}$$

where  $n \in \mathbb{Z}$  and  $d_n$  are undetermined coefficients for fitting.  $\mathbf{v}_n$  is the  $n$ -th nearest neighbor vector which has

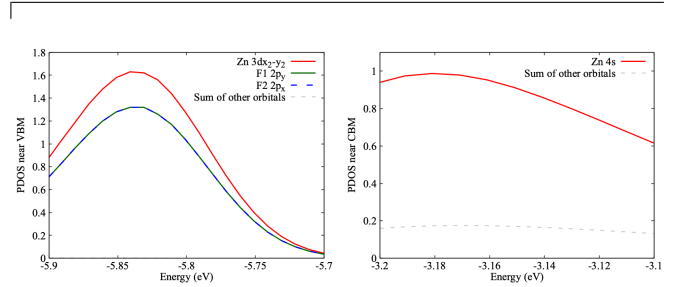


FIG. 11. Left: Projected density of states at the CBM - the dominating orbitals are Zinc  $3d_{x^2-y^2}$  and Floride  $2p_x, 2p_y$ . Right: Projected density of states at VBM, dominating orbital is Zinc  $1s$ . The summation of contributions from all other orbitals in all atoms is significantly smaller than Zn  $1s$ .

the smallest positive angle with respect to the  $x$ -axis:  $\mathbf{v}_1 = (1, 0)$ ,  $\mathbf{v}_2 = (1, 1)$ ,  $\mathbf{v}_3 = (2, 0)$ , etc. And  $C_{4z}^c \cdot \mathbf{v}_n$  is the action of fourfold rotation on vector  $\mathbf{v}_n$  by  $c$ -times. For each position  $\mathbf{x}$ , the optimal  $d_z$  is found by minimizing the total bilayer energy - the latter first decrease and then increase with respect to the interlayer distance. The parameters in equation (41) are fitted to be (in units of meV):

$$\begin{aligned}
d_0 &= 723.75, & d_1 &= 36.9956, & d_2 &= 4.91071, \\
d_3 &= 38.7193, & d_4 &= 2.13811.
\end{aligned} \tag{42}$$

We plot the spatial profile of  $d_z$  in fig. 12.

The symmetry-allowed intralayer and interlayer moiré potentials (defined in (1)) can also be expanded in harmonics,

$$\begin{aligned}
V(\mathbf{x}) &= V_0 + \sum_{n=1} V_n \left[ \sum_{c=0}^3 \cos(2\pi\mathbf{x} \cdot (C_{4z}^c \cdot \mathbf{v}_n)) \right] \\
T(\mathbf{x}) &= T_0 + \sum_{n=1} T_n \left[ \sum_{c=0}^3 \cos(2\pi\mathbf{x} \cdot (C_{4z}^c \cdot \mathbf{v}_n)) \right],
\end{aligned} \tag{43}$$

For example, when  $n = 1$ , we just get back the terms in (2). The numbers for  $V_n$  and  $T_n$ 's are presented in table II.

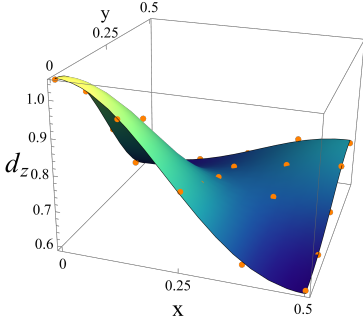


FIG. 12. Optimal interlayer distance as a function of relative shift between layers in the first quadrant.

#### D. Coulomb interactions in ZnF<sub>2</sub>

The quartic terms in the effective moiré Hubbard model of twisted bilayer ZnF<sub>2</sub> can be estimated from the Wannier functions. We assume the interactions are screened by top and bottom metallic gates, separated from the sample with distance  $\xi$ , such that the Coulomb interaction is

$$\begin{aligned} U_{o\sigma'}(\mathbf{d}) &= \int d^2\mathbf{x}d^2\mathbf{x}' |\psi_o(\mathbf{x} - \mathbf{d})|^2 V(\mathbf{x} - \mathbf{x}') |\psi_{\sigma'}(\mathbf{x}')|^2 \\ &= \int \frac{d^2\mathbf{q}}{(2\pi)^2} \rho_o(\mathbf{q}) \rho_{\sigma'}(-\mathbf{q}) \frac{e^2}{2\epsilon\epsilon_0 q} \tanh(q\xi) e^{-i\mathbf{q}\cdot\mathbf{d}}, \end{aligned} \quad (44)$$

where  $V(\mathbf{x} - \mathbf{x}') = \frac{e^2}{\epsilon_0\epsilon|\mathbf{x} - \mathbf{x}'|}$  and  $\epsilon$  is taken to be 10 throughout. The orbitals  $o, \sigma'$  can be  $s, p_x, p_y$ . Similarly, the onsite Hund's coupling  $J$  for the  $p$ -orbital is

$$\begin{aligned} J_{p_x, p_y} &= \int d^2\mathbf{x}d^2\mathbf{x}' \psi_{p_x}^*(\mathbf{x}) \psi_{p_y}(\mathbf{x}) \\ &\quad V(\mathbf{x} - \mathbf{x}') \psi_{p_y}^*(\mathbf{x}') \psi_{p_x}(\mathbf{x}'). \end{aligned} \quad (45)$$

In fig. 13, we plot the nearest neighbor Coulomb interactions  $U_A = U_{p_x p_x}(a_m, 0)$ ,  $U_B = U_{p_x p_y}(a_m, 0)$ ,  $U_C = U_{p_x p_x}(0, a_m)$  as a function of twisting angle.

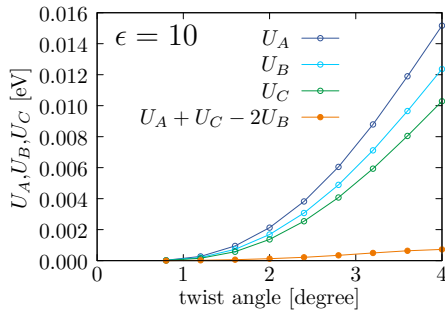


FIG. 13.  $U_A + U_C - 2U_B > 0$  indicates antiferro-orbital order, consistent with the analysis in section III C.

#### E. Hartree-Fock details

The relevant interaction terms for the  $p$ -orbitals in equation (14) can be re-organized as

$$\begin{aligned} H_{\text{onsite}} &= \frac{1}{2} \sum_{a,\sigma} \left[ U n_{a\sigma} n_{a\bar{\sigma}} - J c_{a\sigma}^\dagger c_{\bar{a}\bar{\sigma}} c_{a\bar{\sigma}}^\dagger c_{\bar{a}\sigma} \right. \\ &\quad \left. + \sum_{\sigma'} \left( U' n_{a\sigma} n_{\bar{a}\sigma'} - J c_{a\sigma}^\dagger c_{a\sigma'} c_{\bar{a}\sigma'}^\dagger c_{\bar{a}\sigma} \right) \right], \end{aligned} \quad (46)$$

The mean field tensors are defined as  $\rho_{a\sigma, a'\sigma'} = \langle c_{a\sigma}^\dagger c_{a'\sigma'} \rangle$ . The range of twisting angles we focus on is  $2.4^\circ \leq \theta \leq 5.1^\circ$ , such that  $1 < U/t_\sigma < 100$ . We reset the hopping amplitude  $t_\sigma = 1$ , and all the other parameters  $t_\pi, U, U', J$  are renormalized to be  $t_\pi/t_\sigma, U/t_\sigma, U'/t_\sigma, J/t_\sigma$ . The system size is chosen to be  $140 \times 140$ . To ensure a robust Hartree-Fock procedure to find the global instead of local minimum, we incorporate the following strategy for the consistent mean field theory solution:

- (i) For a variety of idealized initial ansätze with different symmetry breaking patterns (which include Néel order, ferromagnetic order, ferro-orbital and antiferro-orbital order, spin/orbital stripe order, charge density waves, and coexistence of those), as well as 20 random ansätze, first run the standard self-consistent calculation for each parameter combinations to obtain an initial set  $\mathcal{S}_1$  of converged low-energy solutions.
- (ii) In each run, tolerance of  $10^{-5}$  is set for convergence. We exploit a temperature annealing schedule to avoid getting trapped in the first local minimum the algorithm finds. The inverse temperature  $\beta$  is initially set to 5, then at iteration 25,  $\beta$  is increased to 15, and then at iteration 75,  $\beta$  is increased to 50. We also utilize the Direct Inversion in the Iterative Subspace (DIIS) convergence acceleration technique [60, 61], which incorporates a history of previous solutions and the corresponding errors, and choose the new solution to be the best linear combination of previous solutions which makes the corresponding error as close to zero as possible. This is to avoid oscillations and slow convergence that can arise from simple linear mixing between input and output solutions.
- (iii) For parameters  $\{t_y(\theta), U(\theta), U'(\theta), J(\theta)\}$ , use the solutions in  $\mathcal{S}_1$  from the neighboring twisting angles  $\theta - \Delta\theta$  and  $\theta + \Delta\theta$  as the initial guesses for the new calculation with angle  $\theta$ . This refinement run is to prevent the case where the idealized initial ansätze for certain phases do not lead to converged solutions in that phase, while an imperfect solution in that phase actually exists. This step will lead to an additional set of solutions  $\mathcal{S}_2$ .

- (iv) For each previously found solution in sets  $\mathcal{S}_1, \mathcal{S}_2$ , we calculate the order parameters and assign it a label (e.g., “Spin-AFM”, “CDW”, “Orbital-Ferro”). For each label, we store the single solution with the highest order parameter magnitude it has found anywhere on the phase diagram. Then for all twisting angles, we use these global champions in each phase as the initial ansätze. This gives yet another additional set of solutions  $\mathcal{S}_3$ . This step is added because there might be phases isolated in a corner of the phase diagram and the previous refinement runs may not be able to capture such candidates at the opposite corners.

The sets  $\mathcal{S}_1, \mathcal{S}_2, \mathcal{S}_3$  will then be merged to find the lowest energy state.

Fig. 14 plots the energies as a function of twisting angle of low-energy solutions with different unit cell types.

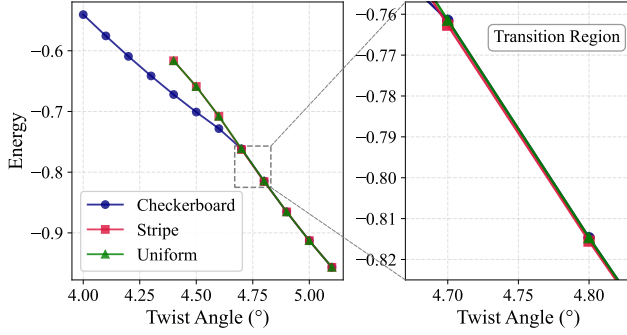


FIG. 14. Total energy as a function of twisting angle near the transition regions. The separation between the stripe geometry and other geometries is of order  $10^{-3}$ , while the error bar is of order  $10^{-5}$ .

Fig. 15 plots additional flavor-resolved band structures complementary to figure 9 in the main text.

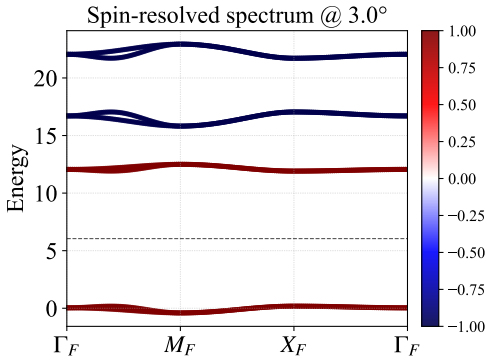


FIG. 15. Spin resolved band structure at  $\theta = 3.0^\circ$  in the folded moiré Brillouin zone which corresponds to the checkerboard unit cell. The lowest bands are spin polarized.

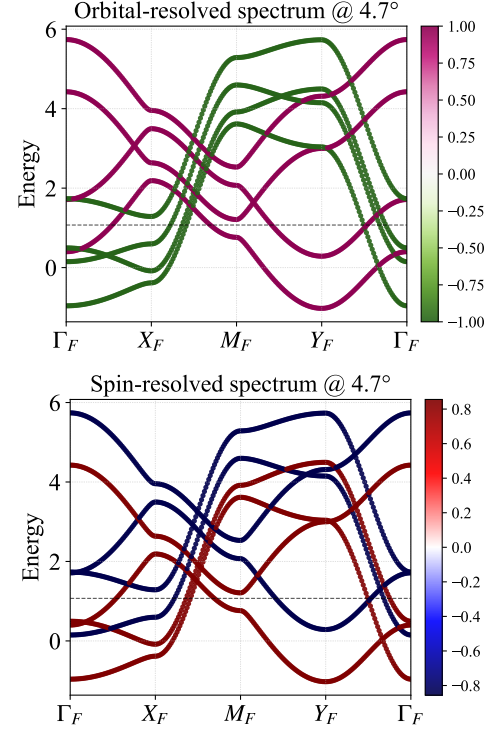


FIG. 16. Flavor resolved band structures at  $\theta = 4.7^\circ$  in the folded moiré Brillouin zone which corresponds to the stripe geometry.

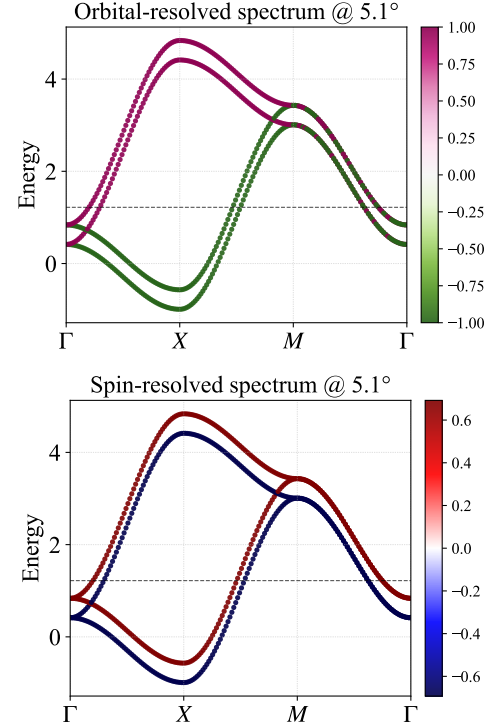


FIG. 17. Flavor resolved band structures at  $\theta = 5.1^\circ$  in the unfolded moiré Brillouin zone.

- [1] Y. Cao, V. Fatemi, S. Fang, K. Watanabe, T. Taniguchi, E. Kaxiras, and P. Jarillo-Herrero, Unconventional superconductivity in magic-angle graphene superlattices, *Nature* **556**, 43 (2018).
- [2] M. Yankowitz, S. Chen, H. Polshyn, Y. Zhang, K. Watanabe, T. Taniguchi, D. Graf, A. F. Young, and C. R. Dean, Tuning superconductivity in twisted bilayer graphene, *Science* **363**, 1059 (2019), <https://www.science.org/doi/pdf/10.1126/science.aav1910>.
- [3] X. Lu, P. Stepanov, W. Yang, M. Xie, M. A. Aamir, I. Das, C. Urgell, K. Watanabe, T. Taniguchi, G. Zhang, *et al.*, Superconductors, orbital magnets and correlated states in magic-angle bilayer graphene, *Nature* **574**, 653 (2019).
- [4] J. M. Park, Y. Cao, K. Watanabe, T. Taniguchi, and P. Jarillo-Herrero, Tunable strongly coupled superconductivity in magic-angle twisted trilayer graphene, *Nature* **590**, 249 (2021).
- [5] Z. Hao, A. M. Zimmerman, P. Ledwith, E. Khalaf, D. H. Najafabadi, K. Watanabe, T. Taniguchi, A. Vishwanath, and P. Kim, Electric field-tunable superconductivity in alternating-twist magic-angle trilayer graphene, *Science* **371**, 1133 (2021), <https://www.science.org/doi/pdf/10.1126/science.abg0399>.
- [6] J. M. Park, Y. Cao, L.-Q. Xia, S. Sun, K. Watanabe, T. Taniguchi, and P. Jarillo-Herrero, Robust superconductivity in magic-angle multilayer graphene family, *Nature Materials* **21**, 877 (2022).
- [7] G. Chen, A. L. Sharpe, P. Gallagher, I. T. Rosen, E. J. Fox, L. Jiang, B. Lyu, H. Li, K. Watanabe, T. Taniguchi, *et al.*, Signatures of tunable superconductivity in a trilayer graphene moiré superlattice, *Nature* **572**, 215 (2019).
- [8] H. Zhou, T. Xie, T. Taniguchi, K. Watanabe, and A. F. Young, Superconductivity in rhombohedral trilayer graphene, *Nature* **598**, 434 (2021).
- [9] H. Kim, Y. Choi, C. Lewandowski, A. Thomson, Y. Zhang, R. Polski, K. Watanabe, T. Taniguchi, J. Alicea, and S. Nadj-Perge, Evidence for unconventional superconductivity in twisted trilayer graphene, *Nature* **606**, 494 (2022).
- [10] Y. Xia, Z. Han, K. Watanabe, T. Taniguchi, J. Shan, and K. F. Mak, **Unconventional superconductivity in twisted bilayer wse<sub>2</sub>** (2024), [arXiv:2405.14784](https://arxiv.org/abs/2405.14784) [cond-mat.mes-hall].
- [11] Y. Guo, J. Pack, J. Swann, L. Holtzman, M. Cothrine, K. Watanabe, T. Taniguchi, D. Mandrus, K. Barmak, J. Hone, A. J. Millis, A. N. Pasupathy, and C. R. Dean, **Superconductivity in twisted bilayer wse<sub>2</sub>** (2024), [arXiv:2406.03418](https://arxiv.org/abs/2406.03418) [cond-mat.mes-hall].
- [12] C. Proust and L. Taillefer, The remarkable underlying ground states of cuprate superconductors, *Annual Review of Condensed Matter Physics* **10**, 409 (2019).
- [13] R. M. Fernandes, A. I. Coldea, H. Ding, I. R. Fisher, P. Hirschfeld, and G. Kotliar, Iron pnictides and chalcogenides: a new paradigm for superconductivity, *Nature* **601**, 35 (2022).
- [14] Q. Si, R. Yu, and E. Abrahams, High-temperature superconductivity in iron pnictides and chalcogenides, *Nature Reviews Materials* **1**, 1 (2016).
- [15] G. Zhou, W. Lv, H. Wang, Z. Nie, Y. Chen, Y. Li, H. Huang, W.-Q. Chen, Y.-J. Sun, Q.-K. Xue, *et al.*, Ambient-pressure superconductivity onset above 40 k in (la, pr) 3ni<sub>2</sub>o<sub>7</sub> films, *Nature* **640**, 641 (2025).
- [16] Y. Soeda, K. Asaga, and T. Fukui, Moiré Landau levels of a C<sub>4</sub>-symmetric twisted bilayer system in the absence of a magnetic field, *Phys. Rev. B* **105**, 165422 (2022).
- [17] Z.-X. Luo, C. Xu, and C.-M. Jian, Magic continuum in a twisted bilayer square lattice with staggered flux, *Phys. Rev. B* **104**, 035136 (2021).
- [18] T. Kariyado and A. Vishwanath, Flat band in twisted bilayer Bravais lattices, *Phys. Rev. Res.* **1**, 033076 (2019).
- [19] M.-R. Li, A.-L. He, and H. Yao, Magic-angle twisted bilayer systems with quadratic band touching: Exactly flat bands with high Chern number, *Phys. Rev. Res.* **4**, 043151 (2022).
- [20] O. Can, T. Tummuru, R. P. Day, I. Elfimov, A. Damascelli, and M. Franz, High-temperature topological superconductivity in twisted double-layer copper oxides, *Nature Physics* **17**, 519 (2021).
- [21] S. Y. F. Zhao, X. Cui, P. A. Volkov, H. Yoo, S. Lee, J. A. Gardener, A. J. Akey, R. Engelke, Y. Ronen, R. Zhong, G. Gu, S. Plugge, T. Tummuru, M. Kim, M. Franz, J. H. Pixley, N. Poccia, and P. Kim, Time-reversal symmetry breaking superconductivity between twisted cuprate superconductors, *Science* **382**, 1422 (2023), <https://www.science.org/doi/pdf/10.1126/science.abl8371>.
- [22] X.-Y. Song, Y.-H. Zhang, and A. Vishwanath, Doping a moiré Mott insulator: A  $t - j$  model study of twisted cuprates, *Phys. Rev. B* **105**, L201102 (2022).
- [23] R. Haenel, T. Tummuru, and M. Franz, Incoherent tunneling and topological superconductivity in twisted cuprate bilayers, *Phys. Rev. B* **106**, 104505 (2022).
- [24] P. A. Volkov, J. H. Wilson, K. P. Lucht, and J. H. Pixley, Current- and field-induced topology in twisted nodal superconductors, *Phys. Rev. Lett.* **130**, 186001 (2023).
- [25] P. M. Eugenio and O. Vafek, Twisted-bilayer FeSe and the Fe-based superlattices, *SciPost Phys.* **15**, 081 (2023).
- [26] A. González-Tudela and J. I. Cirac, Cold atoms in twisted-bilayer optical potentials, *Phys. Rev. A* **100**, 053604 (2019).
- [27] T. Salamon, A. Celi, R. W. Chhajlany, I. Frérot, M. Lewenstein, L. Tarruell, and D. Rakshit, Simulating twistrionics without a twist, *Phys. Rev. Lett.* **125**, 030504 (2020).
- [28] Z. Meng, L. Wang, W. Han, F. Liu, K. Wen, C. Gao, P. Wang, C. Chin, and J. Zhang, Atomic Bose-Einstein condensate in twisted-bilayer optical lattices, *Nature* **615**, 231 (2023).
- [29] Q. Fu, P. Wang, C. Huang, Y. V. Kartashov, L. Torner, V. V. Konotop, and F. Ye, Optical soliton formation controlled by angle twisting in photonic moiré lattices, *Nature Photonics* **14**, 663 (2020).
- [30] P. Wang, Y. Zheng, X. Chen, C. Huang, Y. V. Kartashov, L. Torner, V. V. Konotop, and F. Ye, Localization and delocalization of light in photonic moiré lattices, *Nature* **577**, 42 (2020).
- [31] B. Lou, N. Zhao, M. Minkov, C. Guo, M. Orenstein, and S. Fan, Theory for twisted bilayer photonic crystal slabs, *Phys. Rev. Lett.* **126**, 136101 (2021).
- [32] Z. Jiang, J. Liu, S. Zheng, G. Duan, and B. Xia, Phononic twisted moiré lattice with quasicryst-

- talline patterns, *Applied Physics Letters* **121**, 142202 (2022), [https://pubs.aip.org/aip/apl/article-pdf/doi/10.1063/5.0109404/16483255/142202\\_1\\_online.pdf](https://pubs.aip.org/aip/apl/article-pdf/doi/10.1063/5.0109404/16483255/142202_1_online.pdf).
- [33] P. M. Eugenio, Z.-X. Luo, A. Vishwanath, and P. A. Volkov, Tunable  $t - t' - u$  hubbard models in twisted square homobilayers, *Phys. Rev. Lett.* **134**, 236503 (2025).
- [34] T. Kariyado, A. Vishwanath, and Z.-X. Luo, Single-band square-lattice hubbard model from twisted bilayer  $c_{568}$ , *Phys. Rev. B* **112**, 125159 (2025).
- [35] Q. Xu, N. Tancogne-Dejean, E. V. Boström, D. M. Kennes, M. Claassen, A. Rubio, and L. Xian, *Engineering 2d square lattice hubbard models in  $90^\circ$  twisted ge/snx ( $x=s, se$ ) moiré superlattices* (2024), [arXiv:2406.05626 \[cond-mat.str-el\]](https://arxiv.org/abs/2406.05626).
- [36] S. Raghu, X.-L. Qi, C.-X. Liu, D. J. Scalapino, and S.-C. Zhang, Minimal two-band model of the superconducting iron oxypnictides, *Phys. Rev. B* **77**, 220503 (2008).
- [37] M. Daghofer, A. Moreo, J. A. Riera, E. Arrighoni, D. J. Scalapino, and E. Dagotto, Model for the magnetic order and pairing channels in fe pnictide superconductors, *Phys. Rev. Lett.* **101**, 237004 (2008).
- [38] A. Moreo, M. Daghofer, J. A. Riera, and E. Dagotto, Properties of a two-orbital model for oxypnictide superconductors: Magnetic order,  $B_{2g}$  spin-singlet pairing channel, and its nodal structure, *Phys. Rev. B* **79**, 134502 (2009).
- [39] P. A. Lee and X.-G. Wen, Spin-triplet  $\langle \mathbf{m} \rangle$  wave pairing in a three-orbital model for iron pnictide superconductors, *Physical Review B* **78**, 10.1103/physrevb.78.144517 (2008).
- [40] K. Kuroki, S. Onari, R. Arita, H. Usui, Y. Tanaka, H. Kontani, and H. Aoki, Unconventional pairing originating from the disconnected fermi surfaces of superconducting  $\text{LaFeAsO}_{1-x}\text{F}_x$ , *Physical Review Letters* **101**, 10.1103/physrevlett.101.087004 (2008).
- [41] F. Wang, H. Zhai, Y. Ran, A. Vishwanath, and D.-H. Lee, Functional renormalization-group study of the pairing symmetry and pairing mechanism of the fe-based high-temperature superconductor, *Physical Review Letters* **102**, 10.1103/physrevlett.102.047005 (2009).
- [42] F. Wang, H. Zhai, Y. Ran, A. Vishwanath, and D.-H. Lee, A numerical renormalization group study of the superconducting and spin density wave instabilities in  $\text{mf}_{1-x}\text{f}_x$  compounds, [arXiv preprint arXiv:0805.3343](https://arxiv.org/abs/0805.3343) (2008).
- [43] M. Arzamasovs and B. Liu, Tight-binding tunneling amplitude of an optical lattice, *European Journal of Physics* **38**, 065405 (2017).
- [44] Y. Jiang, U. Petralanda, G. Skorupskii, Q. Xu, H. Pi, D. Călugăru, H. Hu, J. Xie, R. A. Mustaf, P. Höhn, V. Haase, M. G. Vergniory, M. Claassen, L. Elcoro, N. Regnault, J. Shan, K. F. Mak, D. K. Efetov, E. Morosan, D. M. Kennes, A. Rubio, L. Xian, C. Felser, L. M. Schoop, and B. A. Bernevig, *2d theoretically twistable material database* (2024), [arXiv:2411.09741 \[cond-mat.mtrl-sci\]](https://arxiv.org/abs/2411.09741).
- [45] D. Campi, N. Mounet, M. Gibertini, G. Pizzi, and N. Marzari, Expansion of the materials cloud 2d database, *ACS Nano* **17**, 11268 (2023), pMID: 37310789, <https://doi.org/10.1021/acsnano.2c11510>.
- [46] G. Meyer and N. Böhmer, Korrosion von messing und bronze durch ammoniumhalogenide, *Zeitschrift für anorganische und allgemeine Chemie* **626**, 1332 (2000).
- [47] N. Marzari and D. Vanderbilt, Maximally localized generalized wannier functions for composite energy bands, *Phys. Rev. B* **56**, 12847 (1997).
- [48] V. V. Mazurenko, S. L. Skornyakov, A. V. Kozhevnikov, F. Mila, and V. I. Anisimov, Wannier functions and exchange integrals: The example of  $\text{LiCu}_2\text{O}_2$ , *Phys. Rev. B* **75**, 224408 (2007).
- [49] Y. Yang, Y. Yang, M. A. Morales, and S. Zhang, *Engineering hubbard models with gated two-dimensional moiré systems* (2025), [arXiv:2508.13314 \[cond-mat.str-el\]](https://arxiv.org/abs/2508.13314).
- [50] J.-Y. P. Delannoy, M. J. P. Gingras, P. C. W. Holdsworth, and A.-M. S. Tremblay, Low-energy theory of the  $t - t' - t'' - u$  hubbard model at half-filling: Interaction strengths in cuprate superconductors and an effective spin-only description of  $\text{la}_2\text{cuo}_4$ , *Phys. Rev. B* **79**, 235130 (2009).
- [51] Y. Zhang, H. Pi, J. Liu, W. Miao, Z. Qi, N. Regnault, H. Weng, X. Dai, B. A. Bernevig, Q. Wu, and J. Yu, *Universal moiré-model-building method without fitting: Application to twisted  $\text{mote}_2$  and  $\text{wse}_2$*  (2024), [arXiv:2411.08108 \[cond-mat.mes-hall\]](https://arxiv.org/abs/2411.08108).
- [52] Y. Li, E. H. Lieb, and C. Wu, Exact results for itinerant ferromagnetism in multiorbital systems on square and cubic lattices, *Phys. Rev. Lett.* **112**, 217201 (2014).
- [53] S. Xu, Y. Li, and C. Wu, Sign-problem-free quantum monte carlo study on thermodynamic properties and magnetic phase transitions in orbital-active itinerant ferromagnets, *Phys. Rev. X* **5**, 021032 (2015).
- [54] F. W. Olver, *NIST handbook of mathematical functions hardback and CD-ROM* (Cambridge university press, 2010).
- [55] P. Giannozzi, S. Baroni, N. Bonini, M. Calandra, R. Car, C. Cavazzoni, D. Ceresoli, G. L. Chiarotti, M. Cococcioni, I. Dabo, A. Dal Corso, S. de Gironcoli, S. Fabris, G. Fratesi, R. Gebauer, U. Gerstmann, C. Gougoussis, A. Kokalj, M. Lazzeri, L. Martin-Samos, N. Marzari, F. Mauri, R. Mazzarello, S. Paolini, A. Pasquarello, L. Paulatto, C. Sbraccia, S. Scandolo, G. Sclauzero, A. P. Seitsonen, A. Smogunov, P. Umari, and R. M. Wentzcovitch, Quantum espresso: a modular and open-source software project for quantum simulations of materials, *Journal of Physics: Condensed Matter* **21**, 395502 (2009).
- [56] P. Giannozzi, O. Andreussi, T. Brumme, O. Bunau, M. Buongiorno Nardelli, M. Calandra, R. Car, C. Cavazzoni, D. Ceresoli, M. Cococcioni, N. Colonna, I. Carnimeo, A. Dal Corso, S. de Gironcoli, P. Delugas, R. A. DiStasio, A. Ferretti, A. Floris, G. Fratesi, G. Fugallo, R. Gebauer, U. Gerstmann, F. Giustino, T. Gorni, J. Jia, M. Kawamura, H.-Y. Ko, A. Kokalj, E. Küçükbenli, M. Lazzeri, M. Marsili, N. Marzari, F. Mauri, N. L. Nguyen, H.-V. Nguyen, A. Otero-de-la Roza, L. Paulatto, S. Poncá, D. Rocca, R. Sabatini, B. Santra, M. Schlipf, A. P. Seitsonen, A. Smogunov, I. Timrov, T. Thonhauser, P. Umari, N. Vast, X. Wu, and S. Baroni, Advanced capabilities for materials modelling with quantum espresso, *Journal of Physics: Condensed Matter* **29**, 465901 (2017).
- [57] I. Hamada, van der waals density functional made accurate, *Phys. Rev. B* **89**, 121103 (2014).
- [58] A. Dal Corso, Pseudopotentials periodic table: From h

- to pu, *Computational Materials Science* **95**, 337 (2014).
- [59] Psl library, .
- [60] P. Pulay, Convergence acceleration of iterative sequences. the case of scf iteration, *Chemical Physics Letters* **73**, 393 (1980).
- [61] P. Pulay, Improved scf convergence acceleration, *Journal of Computational Chemistry* **3**, 556 (1982).